NANO LETTERS
Letter
Cite This: Nano Lett. 2019, 19, 1052−1060
pubs.acs.org/NanoLett

Gate Tunable Hole Charge Qubit Formed in a Ge/Si Nanowire Double Quantum Dot Coupled to Microwave Photons

Rui Wang,[†,‡] Russell S. Deacon,[*,†,§] Jian Sun,[†,∥] Jun Yao,[⊥] Charles M. Lieber,[#,¶] and Koji Ishibashi[†,§]

[†]Advanced Device Laboratory, RIKEN, Wako, Saitama 351-0198, Japan
[‡]Department of Physics, Tokyo University of Science, Kagurazaka, Tokyo 162-8601, Japan
[§]Center for Emergent Matter Science (CEMS), RIKEN, Wako, Saitama 351-0198, Japan
[∥]Hunan Key Laboratory of Super Micro-Structure and Ultrafast Process, School of Physics and Electronics, Central South University, Changsha 410083, China
[⊥]Department of Electrical and Computer Engineering, Institute for Applied Life Sciences, University of Massachusetts, Amherst, Massachusetts 01003, United States
[#]Deparment of Chemistry and Chemical Biology, Harvard University, Cambridge, Massachusetts 02138, United States
[¶]School of Engineering and Applied Sciences, Harvard University, Cambridge, Massachusetts 02138, United States

Supporting Information

ABSTRACT: A controllable and coherent light-matter interface is an essential element for a scalable quantum information processor. Strong coupling to an on-chip cavity has been accomplished in various electron quantum dot systems, but rarely explored in the hole systems. Here we demonstrate a hybrid architecture comprising a microwave transmission line resonator controllably coupled to a hole charge qubit formed in a Ge/Si core/shell nanowire (NW), which is a natural one-dimensional hole gas with a strong spin−orbit interaction (SOI) and lack of nuclear spin scattering, potentially enabling fast spin manipulation by electric manners and long coherence times. The charge qubit is established in a double quantum dot defined by local electrical gates. Qubit transition energy can be independently tuned by the electrochemical potential difference and the tunnel coupling between the adjacent dots, opening transverse (σ_x) and longitudinal (σ_z) degrees of freedom for qubit operation and interaction. As the qubit energy is swept across the photon level, the coupling with resonator is thus switched on and off, as detected by resonator transmission spectroscopy. The observed resonance dynamics is replicated by a complete quantum numerical simulation considering an efficient charge dipole-photon coupling with a strength up to $2\pi \times 55$ MHz, yielding an estimation of the spin-resonator coupling rate through SOI to be about 10 MHz. The results inspire the future researches on the coherent hole-photon interaction in Ge/Si nanowires.

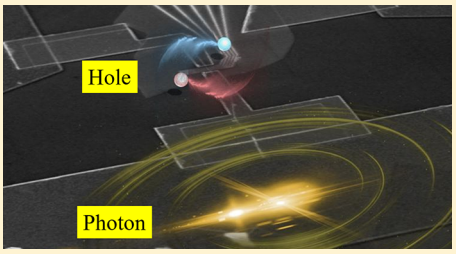

KEYWORDS: *Nanowire, quantum dot, hole qubit, microwave resonator, light-matter interface*

Circuit quantum electrodynamics (cQED) with manufactured quantum bits (or qubits) opens a feasible path for the implementation of solid-state quantum processors, because of the capabilities of flexible design of device geometry, the persistent qubit-cavity interaction, and the lithographic scalability.[1,2] Qubits formed in semiconductor quantum dots (QDs) in the context of cQED,[3,4] i.e., confined electrons or spins, analogous to the superconducting counterparts,[5,6] show promise as a coherent light-matter interface. With fast quantum state manipulation and the potential for long coherence times, which for electron spins in isotopically purified Si have extended to the level of milliseconds,[7,8] a series of recent advances in realizing strong coupling of single electrons and electron spins has been reported,[9−14] all satisfying the essential criterion that the qubit-cavity coupling strength g_c exceeds the qubit decoherence rate γ and the resonator photon loss rate κ.[1] These recent advances toward coherent interaction are mainly facilitated by improving the device coherence (making it more robust to charge noise) to reduce γ[10,15] or employing a high-impedance resonator to elevate the capacitive coupling strength g_c.[11−14] The coherent photon trapped inside cavities can serve as an "information bus" to mediate the interaction between the long-distance qubits or facilitate the communication of separated quantum circuits. The entanglement between the separated superconducting qubits or with the electron ensemble in diamond via a single resonator has been realized.[16−18] Similar results have been demonstrated recently between semiconductor qubits and in a hybrid composite containing a superconducting and a semiconductor qubits.[19,20] So far, all of these inspiring

Received: October 28, 2018
Revised: January 13, 2019
Published: January 14, 2019

DOI: 10.1021/acs.nanolett.8b04343
Nano Lett. 2019, 19, 1052−1060

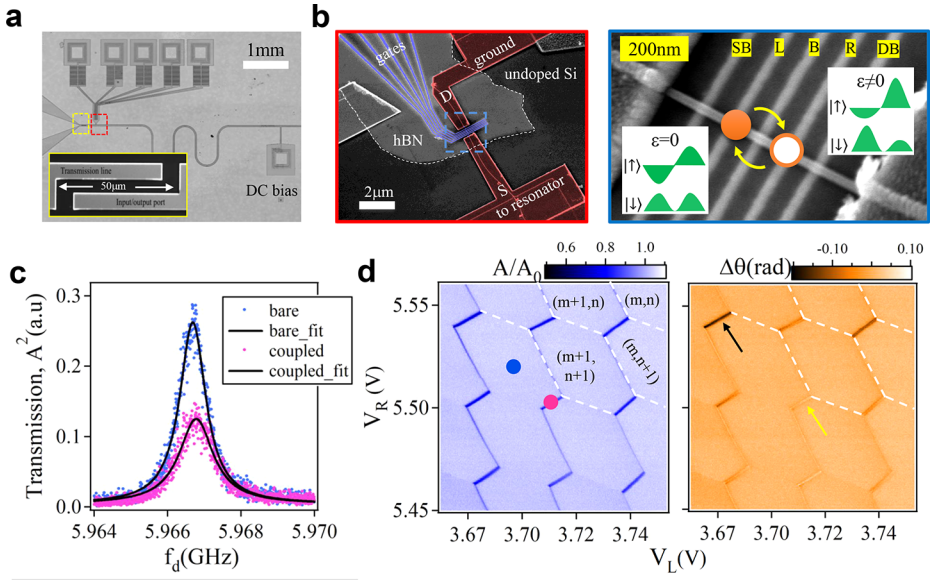

Figure 1. A nanowire-resonator hybrid device. (a) An optical micrograph of the left half panel of a typical superconducting MoRe transmission line resonator. Inset is the magnified scanning electron micrograph (SEM) of the input/output coupler. Close to each open (mirrored) end, the nanowire is deposited onto exfoliated hBN on top of predefined surface gates. The DC wires are connected to the bonding pads through on-chip LC filters. (b) SEM images of the nanowire device with a high magnification. The principle of the charge qubit coupled to the photon field is illustrated. (c) Comparison of the resonance transmission spectra with $\varepsilon = 0$ and $\varepsilon \gg 0$, corresponding to blue and red dots in part d, respectively. (d) Magnitude and phase variation of the transmitted signal as a function of V_L and V_R, representative of a 3 × 3 charge stability diagram. The arrows in the phase shift plot highlight the coexistence of negative and positive signals. The other gate voltages and bias settings are $V_{SB} = 4.3$ V, $V_B = 7.145$ V, $V_{DB} = 3.5$ V, and $V_{sd} = 0$ V.

experiments have concentrated on single electrons and electron spins.[9−14,21−23] To our best knowledge, the experimental demonstration of a hole-based qubit in semiconductor QDs coupled to a circuit cavity has been rarely reported.[24] The coupling strength and the controllability of the hybrid cQED remains unclear and becomes of fundamentally increasing interest.

Here we report a hybrid cQED architecture based on a microwave transmission line resonator coupled to a hole charge qubit formed in a Ge/Si core/shell nanowire (NW), which is a natural one-dimensional hole gas with a high carrier transport mobility and strong spin−orbit interaction (SOI).[25−28] The Ge/Si NW possesses several desirable qualities that may make it suitable as a building block for fault-tolerant quantum information processing. The key properties being that the nature of the group-IV material, the *p*-orbital symmetry of hole wave functions, and state-of-the-art isotopic purification of Ge and Si imply the absence of a hyperfine interaction and hence potentially long spin coherence.[26,29−31] Upon forming the double QD (DQD) along the NW by energizing the local electrical gates, a two-level system (TLS) is defined close to the charge transition degeneracy between the adjacent QDs due to the existence of tunnel coupling. The charge qubit energy can be tuned relative to the cavity photon level using the gates, thus switching on and off the coupling. The variation of the resonance transmission can be utilized as a noninvasive probe to recognize the qubit state in a weak drive limit. A complete quantum numerical simulation is conducted on the hybrid system, providing a comparison to interpret the experimental results. The charge-photon coupling strength is estimated as $g_c = 2\pi \times 35{\sim}55$ MHz, indicating that the holes trapped in the Ge/Si NW DQD can be efficiently coupled to the resonator. However, the observation of strong coupling is prevented due to the existence of a fast qubit decoherence $\gamma = 2\pi \times 4{\sim}6$ GHz. The power dependence of the resonance dispersive shift further reveals that the pure dephasing is orders of magnitude faster than the energy relaxation and is the dominant contribution to the decoherence of the charge qubit. Given the theoretically predicted and experimentally evident short spin−orbit length l_{SO} of the Ge/Si NW,[26−28] the large g_c indicates that a fast and switchable spin-photon interaction g_s might be accessible, according to the linear relation $g_s \propto g_c/l_{SO}$ as several theories have proposed.[29,32]

A typical 50 Ω transmission line resonator (left half panel) fabricated using a 100 nm MoRe superconducting thin film is shown in the micrograph of Figure 1a (Device Preparation in the Supporting Information). Close to each open end (inset of Figure 1a) of the $\lambda/2$ microwave frequency resonator, a Ge/Si NW device was placed bridging the center pin and ground plane in order to maximize the capacitively coupling strength (Figure 1b). Each NW is lying on a set of dense surface gates using an exfoliated hexagonal boron−nitride (hBN) flake as the dielectric layer. The DQD is defined by applying voltages on each finger gate, denoted as V_{SB}, V_L, V_B, V_R, and V_{DB}, respectively. For simplicity, we focused on one NW coupled to the resonator, while the NW at the other end was always pinched off. In the measurements, several tens of holes were contained in each QD because the device was found to be too unstable in the few holes regime. We ignore many body effects and assume a single level in each QD in the model we employ to evaluate our results. Under certain gate conditions, the DQD is isolated from the source-drain electrodes and only the interdot tunneling is allowed. Individual holes trapped in the DQD can be treated as a charge qubit, which can be described by the TLS model[10,33]

DOI: 10.1021/acs.nanolett.8b04343
Nano Lett. 2019, 19, 1052−1060

$$H_{qb} = \frac{1}{2}(\varepsilon\tau_z + 2t_c\tau_x) \quad (1)$$

The qubit energy is given by $E_{qb} = \hbar\omega_{qb} = \sqrt{\varepsilon^2 + (2t_c)^2}$, where $f_{qb} = \omega_{qb}/2\pi$ is the qubit transition frequency, $\hbar$ is the reduced Planck constant, and t_c is the tunnel coupling strength intra-DQD controlled by V_B. $\varepsilon = \mu_L - \mu_R$ represents the energy level difference between the adjacent QDs, and $\mu_{L(R)}$ is the electrochemical potential of each QD tuned by the plunger gate voltages. $\tau_{x,z}$ are the Pauli matrices for the positional bases $|L\rangle$ and $|R\rangle$. The arbitrary charge qubit involves the ground $|\downarrow\rangle$ and excited $|\uparrow\rangle$ states, which are the eigenstates derived from the Hamiltonian in eq 1 after diagonalization. For instance, when $\varepsilon = 0$, the hole is mobile through the intra-QD transitions and equivalently dwells in the left and right dots as illustrated in Figure 1b. The qubit can be encoded by the molecular bonding ($|\downarrow\rangle$) and antibonding states ($|\uparrow\rangle$) in the positional bases given as $(|L\rangle - |R\rangle)/\sqrt{2}$ and $(|L\rangle + |R\rangle)/\sqrt{2}$, respectively. Once the DC plunger gate voltages or the microwave electric field tunes $\varepsilon \neq 0$ (particularly when $\varepsilon \gg t_c$), the hole tends to be trapped in either left or right dot (being localized in the $|L\rangle$ or $|R\rangle$ state), where the charge transition between QDs is forbidden.

The qubit energy will change with respect to t_c and ε controlled by the gate voltages. The corresponding susceptibility of the DQD to microwave photons also varies, allowing the characterization by DC transport and microwave resonance response simultaneously. The transmission of the resonator was investigated by a lock-in homodyne technique at the base temperature of ∼50 mK (measurement setup in Figure S1). Figure 1c presents the comparison of the resonance spectra, where $\varepsilon \gg 0$ (blue dot, Figure 1d) and $\varepsilon = 0$ (red dot, Figure 1d), respectively. The qubit is considered nearly uncoupled to the resonator when QD is in the deep Coulomb blockade regime as the detuning $\varepsilon \gg g_c$. The blue points in Figure 1c are measured when $\varepsilon \gg 0$ and represent a spectrum similar to the bare resonance, showing a Lorentzian line shape with a central frequency $f_c = \omega_c/2\pi = 5.9667$ GHz and a width $\Delta f = \kappa/2\pi = 1$ MHz, yielding a loaded quality factor $Q \sim 6000$. The lifetime of trapped photons in the cavity is $1/\kappa \approx 160$ ns. As the DQD is capacitively coupled to the resonator, we only consider the voltage fluctuation induced by one trapped photon, which is estimated by $V_{rms} = \sqrt{hf_c/C_l l} \approx 1.5$ μV, where $C_l = 1.66 \times 10^{-10}$ F/m is the capacitance per unit length of the waveguide, $l = 10$ mm is the resonator length, and h is the Planck constant.[34]

At $\varepsilon = 0$, the hole is delocalized in the DQD. When t_c is tuned close to the photon energy, the charge qubit becomes susceptible to the microwave electric field. As a result, the central position and the magnitude of the resonance transmission spectrum (red points in Figure 1c) are both altered due to the dispersive pull and the dissipation from the qubit, respectively. Figure 1d plots out the relative magnitude change A/A_0 and phase variations $\Delta\theta = \theta - \theta_0$ as a function of V_L and V_R at a fixed drive frequency $\omega_d/2\pi = f_d = f_c$ with a DC bias of $V_{sd} = 0$. A_0 and θ_0 are the amplitude and phase of the transmitted signal when the DQD is in the deep blockade regime. The power of the probe microwave signal reaching the input port of the resonator is always $P_{in} = -125$ dBm (corresponding to ∼4 photons in the bare resonator, rough estimation with $n \sim P_{in}/hf_c\kappa$),[3,4] unless noted otherwise. In both plots, an array of parallel tilt-dashes is visible. A clear honeycomb-like pattern is observed, as outlined by the white dotted lines, a manifestation of a typical 3 × 3 charge stability diagram of a DQD. Indices m/n in Figure 1d indicate the respective charge number in the left/right dot. The pronounced signals observed at the short boundaries shared by two adjacent hexagons arise from the charge transitions between the left and right dot, where $\varepsilon \approx 0$ and the total charge number of the DQD is a constant. The vertical boundaries of each hexagon are also seen because of the dissipation caused by the charge transition between the nearby (left) dot and the lead connecting to the resonator, whereas the lateral boundaries representing the charge hopping between the far (right) dot and the ground plane are much weaker due to the small capacitive coupling to the resonator. The direct charge transport and the related resonance response are also investigated when the DQD is out-of-equilibrium under finite V_{sd} (Figure S2). The charging energy of each dot is evaluated as $E_L = 2.6$ meV and $E_R = 2.8$ meV. The coupling lever arms of the plunger gates and the source electrode to quantum levels in the DQD are $\alpha_L = 0.079$ eV/V, $\alpha_R = 0.077$ eV/V, and $\alpha_s = 0.243$ eV/V, respectively. The electrochemical potential of each dot considering the mutual capacitive coupling reads $\mu_{L(R)} = \alpha_{L(R)}V_{L(R)} + \beta_m\alpha_{R(L)}V_{R(L)}$, where the cross capacitive coupling rate $\beta_m = C_m/C_{L(R)}^{\Sigma}$, the mutual capacitance between dots $C_m \approx 20$ aF, and $C_{L(R)}^{\Sigma} \approx 60$ aF is the total capacitance of each dot. The vacuum Rabi coupling rate can be roughly estimated as $g_c/2\pi = \alpha_s V_{rms}/h \approx 90$ MHz.[1] We observe both negative and positive phase shifts in the same plot as highlighted by arrows in Figure 1d. Because the phase shift is strongly influenced by the qubit-cavity energy detuning, the coexistence of negative and positive phase shift implies that the qubit is close to resonance with the photons.

We now concentrate on one interdot charge transition line. The evolution of the phase signal for the same range of V_L and V_R is present in Figure 2a with V_B altered in steps of 10 mV. The mean electrochemical potential and energy detuning of the DQD is indicated by the axes as μ and ε, where $\mu = \mu_L + \mu_R$. The values of μ and ε can be converted from the plunger gate voltages and lever arms as previously discussed. Under each V_B condition, the homogeneous phase signals always appear along the interdot lines, where detuning ε is constant. Once the QD is detuned such that $\varepsilon \neq 0$, the phase shift $\Delta\theta$ varies rapidly. In addition, as V_B increases (corresponding to a rise of the middle barrier height E_B and thus a smaller tunneling rate t_c/h), the position in gate voltages of the interdot line is slightly shifted due to the capacitive coupling from the barrier gate. More importantly, we observed that the negative phase shift gradually changes to a positive shift as E_B increases. Traces of $\Delta\theta$ as a function of ε for different V_B are compared in more detail in Figure 2b. Detuning ε is varied by sweeping V_L and V_R along the arrows indicated in Figure 2a. Alongside the observed change of magnitude, the line shape of the phase shift spectra is clearly altered from a single dip as t_c is reduced. We attribute the changes of $\Delta\theta$ to the circumstance that the tunnel coupling rate undergoes an evolution from $2t_c/h > f_c$ to $2t_c/h < f_c$ as V_B (E_B) increases.

To quantitatively interpret the dynamical response of the resonance transmission to the qubit states, we compare the experimental observations with an analytical model from the input−output theory and also a full quantum numerical simulation, and both models show a good consistency with the experiments. Throughout the present work, we first employ the analytical model to fit out the physical parameters such as g_c, γ,

DOI: 10.1021/acs.nanolett.8b04343
Nano Lett. 2019, 19, 1052−1060

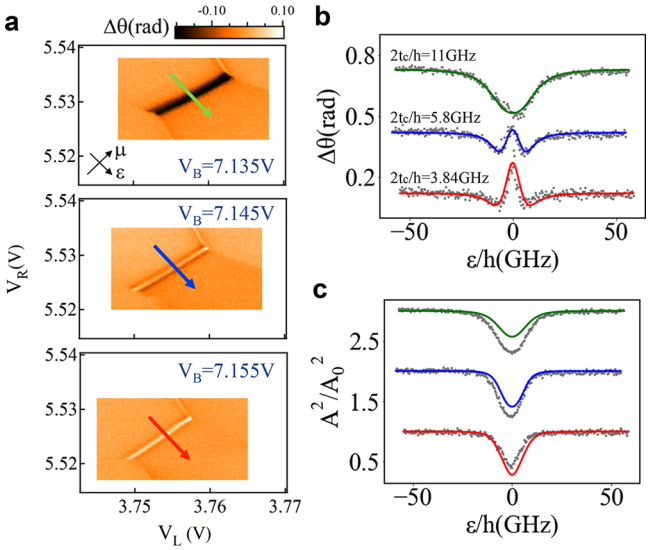

Figure 2. Tuning of the charge qubit energy and the qubit-resonator coupling. (a) Evolution of one interdot charge transition line for the same range of V_L and V_R at zero bias with V_B = 7.135 V (upper), V_B = 7.145 V (middle), V_B = 7.155 V (bottom). Comparison of (b) phase shift $\Delta\theta$ and (c) relative transmission power change A^2/A_0^2 as a function of ε with a different V_B. The gray dotted lines are measured data, and the solid lines are the fits using eq 4. The colors used in parts a and b are correlated with each corresponding to a different V_B. The fitted parameters are $[2t_c/\hbar, g_c, \gamma] = 2\pi \times [11, 0.038, 5.25]$ GHz (green), $2\pi \times [5.8, 0.035, 4.5]$ GHz (blue), and $2\pi \times [3.84, 0.055, 6.49]$ GHz (red), respectively. The traces in parts b and c are vertically offset for clarity.

and t_c. We later conducted the quantum numerical simulation using the fitted-out parameters to reproduce the full transmission spectrum. The hybrid system is modeled by a Jaynes–Cummings (JC)-type Hamiltonian describing a TLS coupled to a single mode photon in a quantized harmonic oscillator:[1,2]

$$H_{JC} = \hbar\omega_c\left(a^\dagger a + \frac{1}{2}\right) + \frac{1}{2}\hbar\omega_{qb}\sigma_z + \hbar g_{eff}(a\sigma^+ + a^\dagger\sigma^-) \tag{2}$$

The first and second terms describe the bare resonator and qubit, respectively. The third term governs the qubit-photon coherent interaction and $g_{eff} = g_c \times 2t_c/E_{qb}$ is the effective coupling rate, which shows a linear relation to the qubit energy. $a^\dagger$ and a are the photon creation and annihilation operators of the single mode resonator. The mean photon number in the resonator is $n = \langle a^\dagger a \rangle$. $\sigma^{+,-}$ are the qubit raising and lowering operators in the energy bases ($|\downarrow\rangle$ and $|\uparrow\rangle$) after the diagonalization of eq 1 and the operator $\sigma_z = |\uparrow\rangle\langle\uparrow| - |\downarrow\rangle\langle\downarrow|$. The expectation value of $\langle\sigma_z\rangle = P_\uparrow - P_\downarrow$defines the qubit occupation probability; here $P_\uparrow = 1 - P_\downarrow = \langle\sigma^+\sigma^-\rangle$ is the qubit excited state population.

For the calculation of transmission spectrum, an external microwave drive is applied on the JC oscillator with an extended Hamiltonian $H = H_{JC} + H_{MW}$, where the coherent drive with an amplitude of ζ at the frequency $f_d = \omega_d/2\pi$ is $H_{MW} = \hbar\zeta(a^\dagger e^{-i\omega_d t} + a e^{i\omega_d t})$. In a rotating frame approximation, we have dropped the rapid oscillating drive term. The system is disturbed by the surrounding environment, leading to dissipation and decoherence. The dynamics of the driven and dissipative system can be described with a density matrix ρ by solving a Markovian master equation:[1,3,35]

$$\dot{\rho} = -\frac{i}{\hbar}[H, \rho] + \mathcal{L}[\rho] \tag{3}$$

Here, $\mathcal{L}[\rho] = \frac{1}{2}\sum_{i=1}^{3}(2C_i\rho C_i^\dagger - C_i^\dagger C_i\rho - \rho C_i^\dagger C_i)$ is the Lindblad operator governing the qubit energy relaxation and dephasing with $C_1 = \sqrt{\gamma_1}\sigma^-$ and $C_2 = \sqrt{\gamma_\Phi/2}\sigma_z$, and the photon dissipation with $C_3 = \sqrt{\kappa}a$.[35] The average value of the photon field $\langle a\rangle = \mathrm{Tr}(a\rho)$ and the qubit occupation probability $\langle\sigma_z\rangle = \mathrm{Tr}(\sigma_z\rho)$ are obtained by extracting the steady state of the hybrid system from eq 3 using the numerical calculation tool, QuTip.[36] As the input/output coupling rate of the resonator is a constant (which is only determined by the design), the output signal from the resonator is linearly proportional to $\langle a\rangle$, from which the magnitude and phase as a function of f_d can be derived. Except for the power dependence experiments, the numerical simulation was implemented in a weak drive limit $\zeta \ll \omega_d$, which is close to the experimental conditions. We restrict the Fock number of photon states N = 2 when the mean photon number trapped in the cavity is smaller than unity. The density matrix ρ is then mapped to a 4 by 4 vector space, which allows an analytical solution using Bloch equations.[3,37] In the power dependence calculation, the Fock space extends to N = 160, limited by our calculation capacity. The photon number changes when the drive amplitude is swept.

We first fit the amplitude and phase response as a function of QD detuning ε in Figure 2b,c using a resonance transmission equation taking into account the decoherence of the qubit and the resonator loss[3,37]

$$t = \frac{-i\kappa_c}{2\pi(f_c - f_d) - i\kappa/2 + g_{eff}^2\langle\sigma_z\rangle/(-2\pi(f_{qb} - f_d) + i\gamma/2)} \tag{4}$$

where κ_c is the input/output coupling rate of the resonator. $\gamma = \gamma_1/2 + \gamma_\Phi$ is the qubit decoherence rate, which is the combination of the energy relaxation rate γ_1 and the pure dephasing rate of superposition states γ_Φ. In a weak drive limit, $\langle\sigma_z\rangle \approx -1$ as the qubit remains predominantly in the ground state. Here we focus on the relative magnitude change A/A_0 and relative phase variation $\Delta\theta$ with respect to the transmission of the bare resonator at the fixed frequency $f_d = f_c$. The numerator of eq 4 can be normalized to unity. Equation 4 was applied to fit the experimental data (gray dotted lines) in Figure 2b. From the evolution of phase spectra with an increasing V_B, we identify that the interdot tunneling rate varies from $2t_c/h$ = 11 GHz > f_c to $2t_c/h$ = 3.84 GHz < f_c. The coupling rate under these gate conditions are in the range $2\pi \times$ 35∼55 MHz, in good agreement with the above estimation with the gate lever arms. With a different t_c, the decoherence rates vary in the range $2\pi \times$ 4.5∼6.5 GHz. (Here we did not consider the ε dependence of the decoherence rate usually observed in a DQD charge qubit.[4,33]) The detailed fitting parameters are present in the figure caption. We also compare the measured A^2/A_0^2 with the calculations from eq 4 using the fitted-out parameters, and the results show a good consistency as shown in Figure 2c. On this device, we did not observe the signature of strong coupling between the qubit and photon, mainly because of the large γ.

The JC system is then numerically simulated with the fitted-out parameters from the results of Figure 2. We first plot out the quantum level spectra of a closed Jaynes–Cummings system for (a) $2t_c/h < f_c$, (b) $2t_c/h = f_c$, and (c) $2t_c/h > f_c$ when

DOI: 10.1021/acs.nanolett.8b04343
Nano Lett. 2019, 19, 1052−1060

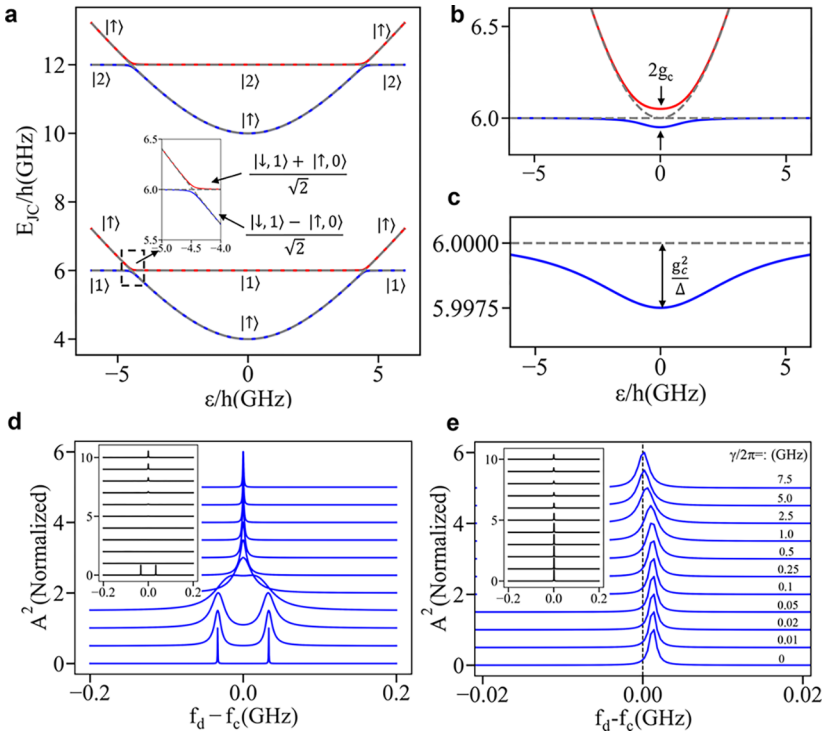

Figure 3. Quantum numerical simulation of the cQED system with a decoherence in a weak drive limit ($\zeta \ll \omega_d$). Energy level spectra of the lowest eigenstates in a closed Jaynes−Cummings system as a function of qubit detuning ε under the condition (a) $2t_c/h < f_c$, (b) $2t_c/h = f_c$, and (c) $2t_c/h > f_c$. The inset of part a indicates the anticrossing levels of a coherent qubit-photon hybridized system encoded by the superposition states, $(|\downarrow, 1\rangle - |\uparrow, 0\rangle)/\sqrt{2}$ and $(|\downarrow, 1\rangle + |\uparrow, 0\rangle)/\sqrt{2}$. The other simulation parameters are $[2t_c/\hbar, g_c, \omega_c, \omega_d, \kappa] = 2\pi \times [4, 0.05, 6, 6, 0.001]$ GHz. The gray dashed lines are the energy spectra of the uncoupled system with $g_c = 0$. The numerically calculated resonator transmission (normalized) with a variable qubit decoherence γ is shown (d) on resonance, $\Delta = 0$, and (e) in the dispersive regime, $f_{qb} = 2t_c/h$ and $\Delta \neq 0$. The inset in parts d and e show the absolute transmission in arbitrary units, presenting the evolution of the dissipation. The traces in parts d and e are vertically offset for clarity.

drive and system decays are not considered. The qubit-cavity energy detuning is defined as $\Delta = h(f_{qb} - f_c)$. The calculated eigenenergies of the four lowest excited states of the hybrid system are presented in Figure 3a. A splitting feature is always observed whenever the qubit energy is swept close to resonance with the photon level as shown in the inset of Figure 3a. The anticrossing gap is determined by the effective coupling rate, g_{eff}. The qubit-photon hybridization is encoded by the superposition states as $(|\downarrow, 1\rangle - |\uparrow, 0\rangle)/\sqrt{2}$ and $(|\downarrow, 1\rangle + |\uparrow, 0\rangle)/\sqrt{2}$. The qubit is repeatedly absorbing/emitting the photon trapped in the cavity, causing a so-called vacuum Rabi splitting.[1,2,5] If $f_{qb} = 2t_c/h = f_c$ as indicated by an arrow in part b, the splitting is at the maximum, equal to $2g_c$. Once the qubit is detuned from the photon level such that $\Delta \neq 0$ (Figure 3c), the system enters a dispersive regime where the cavity mode is shifted by as much as g_{eff}^2/Δ, where the shift is largest at $\varepsilon = 0$.

With a probe drive ($\zeta \sim 0.0001\omega_d$ to ensure the photon number in the cavity is much less than a unity), we are able to calculate the transmitted signal through the resonator. To fully interpret the influence of the qubit decoherence on the dressed qubit and photons, we numerically calculated the transmission spectrum for a range of decoherence rate γ when qubit-cavity is both on resonance, $\Delta = 0$, and detuned, $\Delta \neq 0$, in Figure 3d,e, respectively. The blue lines in the main plots of parts d and e are the normalized spectra and highlight the line shape changes. The absolute transmission spectra (insets of parts d and e) give information about the effects of dissipation from the amplitude variations of the peaks. The corresponding phase spectra are also compared (Figure S3). It is clearly seen that when $\Delta = 0$ two separated peaks always appear when $\gamma < 2g_{eff}$, and they broaden and finally merge into a single peak as γ increases. Once γ becomes much larger than g, the broadened peak narrows as the incoherent interaction dominates. When $\Delta \neq 0$, only a single peak is observed with the central position displaced from f_c, due to the dispersive pull of the qubit. As γ increases, a similar broadening of the peak is seen, while the shift of the peak gradually diminishes toward zero. The simulations are in line with the measurements that a large γ gives rise to the small observed phase shifts. The ε dependence of A^2/A_0^2 and $\Delta\theta$ with a different g and γ are also calculated (Figure S4), providing a comparison to the measured data in Figure 2.

Under the gate condition of $V_B = 7.155$ V corresponding to $2t_c/h = 3.84$ GHz $< f_c$ (red line in Figure 2), we compare the measured transmission as a function of ε and f_d with the numerical simulation in a weak drive limit, as shown in (Figure 4). The absolute and normalized transmitted power from the measurements are presented in parts a and b, respectively. Corresponding numerical calculations using the fitted-out parameters are shown in parts c and d. The simulations replicate the main features of the measurements. For instance, a similar reduction of the transmitted signal is observed where $\varepsilon \approx 0$ (or the detuning Δ is small) in both parts a and c due to the qubit dissipation. Moreover, in the normalized transmission spectra of parts b and d, both positive and negative dispersive shifts on the scale of a few hundred kHz are

DOI: 10.1021/acs.nanolett.8b04343
Nano Lett. 2019, 19, 1052−1060

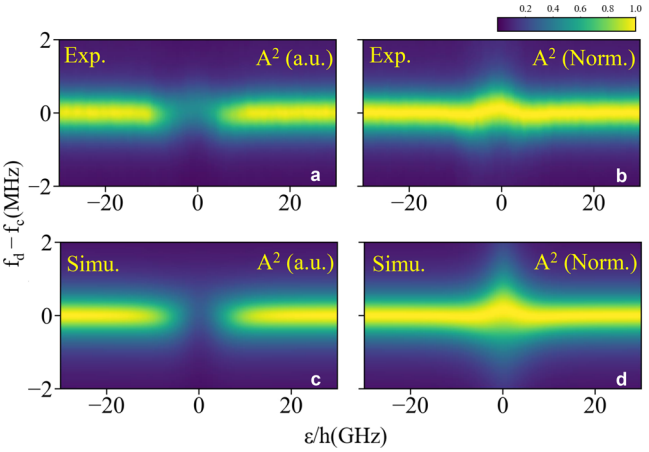

Figure 4. Comparison of experiment and numerical simulation. Full transmission spectrum as a function of f_d and ε with voltage conditions corresponding to the red arrow in Figure 2a. The measured signal is plotted (a) as the absolute transmission power in arbitrary units and (b) normalized transmission power. Plots show a good consistency with the numerical simulations plotted in parts c and d, respectively. Simulations use the exact experimental and fitting parameters. In the simulation, the microwave drive amplitude $\zeta \sim 0.0001\omega_d$ to ensure the photon number in the cavity is much lower than the unity. In the normalized plots, the spectrum at each ε is normalized to its own maximal output power.

observed when the qubit energy is swept. A slight deviation is observed as the simulated peak broadening close to $\varepsilon = 0$ is larger than that of the measurements. The discrepancy may originate from the lower charge noise sensitivity of the real device when the qubit is tuned to the so-called "sweet spot", while in the simulation we used the constant γ.[4,33] The γ dependence of the full transmission spectra is conducted with a numerical simulation and how it hinders the occurrence of the Rabi splitting are discussed in Figure S5.

To separate the influence of the qubit energy relaxation γ_1 and the pure dephasing γ_Φ, we further examine the power dependence of the transmitted signal in a dispersive regime. We first examine the numerical simulation. The calculated $\langle\sigma_z\rangle$ and $\Delta\theta$ as a function of n with a fixed γ but different γ_1 are shown in Figure 5a,b. The physical parameters used for the simulation are $[2t_c/\hbar, \varepsilon, g_c, \gamma, \omega_c, \omega_d] = 2\pi \times [4, 0, 0.05, 6, 6, 6]$ GHz. With an increasing photon number n up to ~120 (where the photon number is numerically calculated out from the input drive amplitude ζ and limited by our workstation calculation capacity), for each γ_1, we observe that $\langle\sigma_z\rangle$ ($\Delta\theta$) consistently increases (decreases) from the minimum (maximum). It is interesting to note that for all γ_1, the initial phase shifts are the same, being only determined by the given γ and Δ, in accordance with the prediction of eq 4. With variable γ, the initial phase proves different as evident by numerical simulation in Figure S6. In contrast, the transition tendencies of $\langle\sigma_z\rangle$ and $\Delta\theta$ are related solely to γ_1, showing a quicker qubit

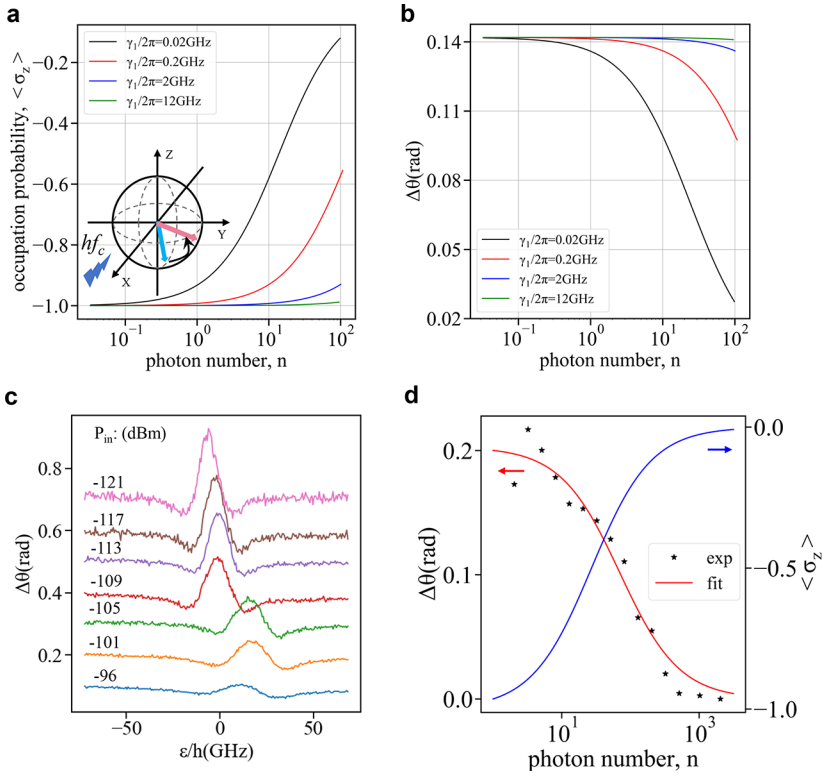

Figure 5. Power dependence of the dispersive shift. Quantum numerical simulation of (a) qubit occupation probability $\langle\sigma_z\rangle$ and (b) phase shift $\Delta\theta$ as a function of cavity photon number n with a fixed γ but different γ_1 in a dispersive regime. n is calculated up to ~120 with a sweeping drive amplitude ζ, limited by our workstation calculation capacity. The other simulation parameters are $[2t_c/\hbar, \varepsilon, g_c, \gamma, \omega_c, \omega_d, \kappa] = 2\pi \times [4, 0, 0.05, 6, 6, 6, 0.001]$ GHz. With a fixed γ, changing γ_1 indicates the variation of γ_Φ, because $\gamma = \gamma_1/2 + \gamma_\Phi$. The inset of part a illustrates the population of the qubit driven by the microwave photon in the Bloch sphere with the energy bases $|\downarrow\rangle$ and $|\uparrow\rangle$ defining the poles of z axis. (c) A series of measured phase shift spectra as a function of ε with a different input drive power P_{in}. The traces are vertically offset for clarity. (d) Measured contrasts of the phase shift $\Delta\theta(\varepsilon = 0) - \Delta\theta(|\varepsilon| \gg 0)$ (dots) are fitted (red line) according to the combination of eqs 4 and 5 as a function of n, giving $\gamma_1 \sim 2\pi \times 70$ MHz, which is much smaller than γ_Φ. The blue line shows the calculated $\langle\sigma_z\rangle$ with eq 5 as a function of n using the fitted-out parameters.

DOI: 10.1021/acs.nanolett.8b04343
Nano Lett. 2019, 19, 1052−1060

saturation (Figure 5a) and phase elimination (Figure 5b) for a smaller γ_1. The ground and excited states of the qubit will be mixed even in the case where $\Delta \neq 0$ due to the qubit transition saturation,[1,38] as illustrated by the Bloch sphere (in the energy bases that $|\downarrow\rangle$ and $|\uparrow\rangle$ define the poles of the z axis) of Figure 5a, where the pointing of the arrow represents the quantum state.

The extent of the qubit state mixing at a given n is also affected by the coherent coupling strength, the qubit-cavity detuning, and the qubit relaxation and decoherence with an analytical relation as[1,38]

$$\langle \sigma_z \rangle = -1/1 + 4g_c{}^2 n\gamma/\gamma_1(\gamma^2 + \Delta^2) \quad (5)$$

Substituting eq 5 into eq 4, we can easily find that the increase of photon number n will reduce the dispersive shift of the resonator, in line with the numerical calculations. The power dependence of the dispersive shift with photon number n (n is an input variable in analytical simulation) is also calculated using eqs 4 and 5, showing the same results as the numerical simulation in Figure S6.

A series of measured $\Delta\theta$ as a function of ε with a different input drive power P_{in} is plotted in Figure 5c, where the qubit state is defined with the same gate conditions indicated by the red arrow in Figure 2. The contrast of the phase shift $\Delta\theta(\varepsilon = 0) - \Delta\theta(|\varepsilon| \gg 0)$ sequentially becomes smaller with an increasing P_{in}. This evolution is further plotted in Figure 5d as a function of n (n spans over 4 orders of magnitude), showing a similar tendency as the numerical simulation in Figure 5a,b. The experimental data was fitted by the combination of eqs 4 and 5 with free γ_1 and γ. The other parameters are fixed with $[2t_c/\hbar, \varepsilon, g_c, \omega_c, \omega_d] = 2\pi \times [3.84, 0, 0.055, 5.9667, 5.9667]$ GHz as determined in the previous analysis. The fitting gives that $\gamma_1 \sim 2\pi \times 70$ MHz and $\gamma \sim 2\pi \times 5$ GHz, yielding the pure dephasing rate $\gamma_\Phi = \gamma - \gamma_1/2 \sim 2\pi \times 5$ GHz, which is orders of magnitude larger than γ_1. The results imply that the inhomogeneous dephasing of the qubit, typically induced by the charge noise, is the main obstacle to the realization of the coherent hole-photon coupling.[4,33] A similar recovery of the bare resonator mode has been experimentally observed when a resonator is coupled to a transmon in a dispersive regime at a large drive power and has been theoretical modeled accounting for the qubit transition saturation.[39−41] A large drive power will also induce the broadening, merging, or even splitting of Rabi peaks when a qubit resonantly couples to the resonator.[42,43]

For the implementation of a strong coupling, further effort must be dedicated to lengthen the qubit coherence. Improving the cleanness of the hBN/NW interface in fabrication or the crystallinity of the NW core and shell in growth may be beneficial to eliminate the unwanted defects and charge impurities. A recent experiment on Si/SiGe quantum dots claims that making an accumulation type QD will help to confine the charge wave function in a compact space, which may make devices less sensitive to the environmental noise.[44] An alternative strategy is to elevate the coupling strength by employing a high-impedance resonator as the vacuum voltage fluctuation $V_{rms} \sim \sqrt{Z_r}$. Following this approach, it has been shown in several recent studies that g_c can be enhanced several fold.[11−13] It is of interest to estimate the potentially effective spin-photon coupling via a spin−orbit interaction based on our current results. As previously reported, the l_{SO} in Ge/Si NWs is short and can be electrically tuned down to a few nanometers,[27,28] which is significantly smaller than the reported values of other materials, for GaAs quantum wells $l_{SO} \sim 20$ μm[45] and for InAs and InSb NWs $l_{SO} \sim 100$ nm.[46,47] In a DQD geometry, we select the qubit energy $E_{qb} = 2t_c = h \times 10$ GHz = 40 μeV at $\varepsilon = 0$ and the half interdot distance $L = 50$ nm. We assume each single dot energy spacing $\Delta E = 0.5$ meV and the corresponding radius of single dot ground state wave function $l = \frac{\hbar}{\sqrt{m^*\Delta E}} \sim 20$ nm, where $m^* = 0.28\ m_0$ is the effective mass of holes and m_0 is the free electron mass.[48] We set $E_Z = hf_c = 24$ μeV, where E_Z is the Zeeman splitting of spin states. Using the reported $g = 2.2$ yields the necessary magnetic field $B = E_Z/g\mu_B \sim 250$ mT, where μ_B is the Bohr magneton.[48] Here we choose a moderate $l_{SO} = 20$ nm (correspondingly a Rashba SOI coefficient $\alpha = \hbar^2/m^* l_{SO} \sim 3 \times 10^{-11}$ eVm) for the Ge/Si NW[27] and $g_c = 2\pi \times 60$ MHz. The spin-photon coupling strength of the DQD is then estimated as $g_s \approx 2g_c(\Delta E E_Z/E_{qb}{}^2)(L/l_{so})\eta \sim 2\pi \times 14$ MHz, $\eta = s/\sqrt{1 - s^2}$ and $s = \langle L \mid R \rangle = e^{-(L/l)^2}$ relates to the interdot wave function overlap.[49] The predicted g_s in the DQD is close to recently reported values of the strong spin-photon coupling using a local magnetic field gradient.[12,13,37] When $\varepsilon \neq 0$, the electron spin is trapped in a single dot, giving the spin-photon coupling strength $g_s \approx g_c(E_Z/\Delta E)(l/l_{so}) \sim 2\pi \times 2.5$ MHz.[3,32] The reasonably large value even for a single QD mainly arises from the short spin−orbit length of Ge/Si NWs. We note that the charge noise can also cause spin decoherence through the SOI. As proposed by Benito et al.,[37] the optimal working point is where the charge qubit is slightly detuned to the photon, for which the charge noise will be largely decoupled to the spin albeit at a cost of reduced spin coupling rate g_s. However, the ratio of spin coupling rate over the decoherence rate g_s/γ_s can be optimized. With the same model as in ref 37, we estimate the spin decoherence rate of our device in a dispersive regime using $\gamma_s = \gamma E_{s\text{-}c}{}^2/4[(E_{qb} - E_Z)^2 + \gamma^2]$, here the spin-charge hybridization energy $E_{s\text{-}c} = \alpha L\eta/l^2 \sim 7.5$ μeV.[49] Using the fitted-out charge decoherence rate $\gamma \sim 2\pi \times 5$ GHz, γ_s is evaluated to be approximately $2\pi \times 120$ MHz, 1 order of magnitude larger than the estimated g_s, indicating that a significant improvement is required to achieve the strong coupling regime. However, if γ can be suppressed to $2\pi \times 100$ MHz (which has been realized in QDs made from a carbon nanotube, Si/SiGe heterostructure, and GaAs quantum well systems[9,10,12−14]), the spin decoherence rate will reduce to $2\pi \times 6$ MHz, allowing access to the strong spin coupling regime.

In conclusion, a controllable cQED system was implemented with a Ge/Si NW DQD embedded in a transmission line resonator. A hole charge qubit is formed at the left−right QD energy degeneracy. The transition energy of the qubit can be tuned across the photon level by local electrical gating, thus turning on and off the coupling, which is detected from the response of the transmitted signal through the cavity. Numerical simulation of the dynamics of the hybrid system provides a powerful guide to interpret the experimental results. The hole-photon coupling strength is evaluated to be in the magnitude of several tens of MHz; however, strong coupling is not achieved due to a fast qubit decoherence. The power dependence of the cavity mode dispersive shift further reveals that pure dephasing dominates the decoherence of the qubit.

DOI: 10.1021/acs.nanolett.8b04343
Nano Lett. 2019, 19, 1052−1060

■ ASSOCIATED CONTENT

Supporting Information

The Supporting Information is available free of charge on the ACS Publications website at DOI: 10.1021/acs.nanolett.8b04343.

Device preparation, measurement setup, DC transport of DQD out of equilibrium, qubit decoherence and coupling strength effects on resonance spectrum, and power dependence of the dispersive shift (PDF)

■ AUTHOR INFORMATION

Corresponding Author

*E-mail: russell@riken.jp.

ORCID

Rui Wang: 0000-0003-2777-3911

Jian Sun: 0000-0002-7992-8092

Jun Yao: 0000-0002-5269-3190

Charles M. Lieber: 0000-0002-6660-2456

Author Contributions

The manuscript was written through contributions of all authors. All authors have given approval to the final version of the manuscript.

Notes

The authors declare no competing financial interest.

■ ACKNOWLEDGMENTS

R.S.D. acknowledges support from Grants-in-Aid for Young Scientists B (26790008) and Grants-in-Aid for Scientific Research (16H02204). J.S. acknowledges support from Grants-in-Aid for Young Scientists (17K14076). The work was partially supported by Grants-in-Aid for Scientific Research (A) (15H02015) and Scientific Research on Innovative Areas "Science of Hybrid Quantum Systems" (15H05867).

■ REFERENCES

(1) Blais, A.; Huang, R.-S.; Wallraff, A.; Girvin, S. M.; Schoelkopf, R. J. Cavity Quantum Electrodynamics for Superconducting Electrical Circuits: An Architecture for Quantum Computation. *Phys. Rev. A: At., Mol., Opt. Phys.* **2004**, *69* (6), 062320.

(2) You, J. Q.; Nori, F. Quantum Information Processing with Superconducting Qubits in a Microwave Field. *Phys. Rev. B: Condens. Matter Mater. Phys.* **2003**, *68* (6), 064509.

(3) Petersson, K. D.; McFaul, L. W.; Schroer, M. D.; Jung, M.; Taylor, J. M.; Houck, A. A.; Petta, J. R. Circuit Quantum Electrodynamics with a Spin Qubit. *Nature* **2012**, *490* (7420), 380−383.

(4) Frey, T.; Leek, P. J.; Beck, M.; Blais, A.; Ihn, T.; Ensslin, K.; Wallraff, A. Dipole Coupling of a Double Quantum Dot to a Microwave Resonator. *Phys. Rev. Lett.* **2012**, *108* (4), 046807.

(5) Wallraff, A.; Schuster, D. I.; Blais, A.; Frunzio, L.; Huang, R.-S.; Majer, J.; Kumar, S.; Girvin, S. M.; Schoelkopf, R. J. Strong Coupling of a Single Photon to a Superconducting Qubit Using Circuit Quantum Electrodynamics. *Nature* **2004**, *431* (7005), 162−167.

(6) Chiorescu, I.; Bertet, P.; Semba, K.; Nakamura, Y.; Harmans, C. J. P. M.; Mooij, J. E. Coherent Dynamics of a Flux Qubit Coupled to a Harmonic Oscillator. *Nature* **2004**, *431* (7005), 159−162.

(7) Muhonen, J. T.; Dehollain, J. P.; Laucht, A.; Hudson, F. E.; Kalra, R.; Sekiguchi, T.; Itoh, K. M.; Jamieson, D. N.; McCallum, J. C.; Dzurak, A. S.; Morello, A. Storing Quantum Information for 30 Seconds in a Nanoelectronic Device. *Nat. Nanotechnol.* **2014**, *9* (12), 986−991.

(8) Veldhorst, M.; Hwang, J. C. C.; Yang, C. H.; Leenstra, A. W.; de Ronde, B.; Dehollain, J. P.; Muhonen, J. T.; Hudson, F. E.; Itoh, K. M.; Morello, A.; Dzurak, A. S. An Addressable Quantum Dot Qubit with Fault-Tolerant Control-Fidelity. *Nat. Nanotechnol.* **2014**, *9* (12), 981−985.

(9) Viennot, J. J.; Dartiailh, M. C.; Cottet, A.; Kontos, T. Coherent Coupling of a Single Spin to Microwave Cavity Photons. *Science* **2015**, *349* (6246), 408−411.

(10) Mi, X.; Cady, J. V.; Zajac, D. M.; Deelman, P. W.; Petta, J. R. Strong Coupling of a Single Electron in Silicon to a Microwave Photon. *Science* **2017**, *355* (6321), 156−158.

(11) Stockklauser, A.; Scarlino, P.; Koski, J. V.; Gasparinetti, S.; Andersen, C. K.; Reichl, C.; Wegscheider, W.; Ihn, T.; Ensslin, K.; Wallraff, A. Strong Coupling Cavity QED with Gate-Defined Double Quantum Dots Enabled by a High Impedance Resonator. *Phys. Rev. X* **2017**, *7* (1), 011030.

(12) Mi, X.; Benito, M.; Putz, S.; Zajac, D. M.; Taylor, J. M.; Burkard, G.; Petta, J. R. A Coherent Spin−Photon Interface in Silicon. *Nature* **2018**, *555* (7698), 599−603.

(13) Samkharadze, N.; Zheng, G.; Kalhor, N.; Brousse, D.; Sammak, A.; Mendes, U. C.; Blais, A.; Scappucci, G.; Vandersypen, L. M. K. Strong Spin-Photon Coupling in Silicon. *Science* **2018**, *359* (6380), 1123−1127.

(14) Landig, A. J.; Koski, J. V.; Scarlino, P.; Mendes, U. C.; Blais, A.; Reichl, C.; Wegscheider, W.; Wallraff, A.; Ensslin, K.; Ihn, T. Coherent Spin−Photon Coupling Using a Resonant Exchange Qubit. *Nature* **2018**, *560* (7717), 179.

(15) Mi, X.; Kohler, S.; Petta, J. R. Electrically Protected Valley-Orbit Qubits in Silicon. *Phys. Rev. B: Condens. Matter Mater. Phys.* **2018**, *98* (16), 161404.

(16) Majer, J.; Chow, J. M.; Gambetta, J. M.; Koch, J.; Johnson, B. R.; Schreier, J. A.; Frunzio, L.; Schuster, D. I.; Houck, A. A.; Wallraff, A.; Blais, A.; Devoret, M. H.; Girvin, S. M.; Schoelkopf, R. J. Coupling Superconducting Qubits via a Cavity Bus. *Nature* **2007**, *449* (7161), 443−447.

(17) Sillanpää, M. A.; Park, J. I.; Simmonds, R. W. Coherent Quantum State Storage and Transfer between Two Phase Qubits via a Resonant Cavity. *Nature* **2007**, *449* (7161), 438−442.

(18) Zhu, X.; Saito, S.; Kemp, A.; Kakuyanagi, K.; Karimoto, S.; Nakano, H.; Munro, W. J.; Tokura, Y.; Everitt, M. S.; Nemoto, K.; Kasu, M.; Mizuochi, N.; Semba, K. Coherent Coupling of a Superconducting Flux Qubit to an Electron Spin Ensemble in Diamond. *Nature* **2011**, *478* (7368), 221−224.

(19) Scarlino, P.; van Woerkom, D. J.; Mendes, U. C.; Koski, J. V.; Landig, A. J.; Andersen, C. K.; Gasparinetti, S.; Reichl, C.; Wegscheider, W.; Ensslin, K.; Ihn, T.; Blais, A.; Wallraff, A. Coherent Microwave Photon Mediated Coupling between a Semiconductor and a Superconductor Qubit. *arXiv* **2018**, *1806*, 10039.

(20) van Woerkom, D. J.; Scarlino, P.; Ungerer, J. H.; Müller, C.; Koski, J. V.; Landig, A. J.; Reichl, C.; Wegscheider, W.; Ihn, T.; Ensslin, K.; Wallraff, A. Microwave Photon-Mediated Interactions between Semiconductor Qubits. *Phys. Rev. X* **2018**, *8* (4), 041018.

(21) Wang, R.; Deacon, R. S.; Car, D.; Bakkers, E. P. a. M.; Ishibashi, K. InSb Nanowire Double Quantum Dots Coupled to a Superconducting Microwave Cavity. *Appl. Phys. Lett.* **2016**, *108* (20), 203502.

(22) Kroll, J. G.; Borsoi, F.; van der Enden, K. L.; Uilhoorn, W.; de Jong, D.; Quintero-Pérez, M.; van Woerkom, D. J.; Bruno, A.; Plissard, S. R.; Car, D.; Bakkers, E. P. A. M.; Cassidy, M. C.; Kouwenhoven, L. P. Magnetic Field Resilient Superconducting Coplanar Waveguide Resonators for Hybrid CQED Experiments. *arXiv* **2018**, *1809*, 03932.

(23) Cottet, A.; Dartiailh, M. C.; Desjardins, M. M.; Cubaynes, T.; Contamin, L. C.; Delbecq, M.; Viennot, J. J.; Bruhat, L. E.; Douçot, B.; Kontos, T. Cavity QED with Hybrid Nanocircuits: From Atomic-like Physics to Condensed Matter Phenomena. *J. Phys.: Condens. Matter* **2017**, *29* (43), 433002.

(24) Li, Y.; Li, S.-X.; Gao, F.; Li, H.-O.; Xu, G.; Wang, K.; Liu, D.; Cao, G.; Xiao, M.; Wang, T.; Zhang, J. J.; Guo, G. C.; Guo, G. P.

DOI: 10.1021/acs.nanolett.8b04343
Nano Lett. 2019, 19, 1052−1060

Coupling a Germanium Hut Wire Hole Quantum Dot to a Superconducting Microwave Resonator. *Nano Lett.* **2018**, *18* (3), 2091−2097.
(25) Xiang, J.; Lu, W.; Hu, Y.; Wu, Y.; Yan, H.; Lieber, C. M. Ge/Si Nanowire Heterostructures as High-Performance Field-Effect Transistors. *Nature* **2006**, *441* (7092), 489−493.
(26) Kloeffel, C.; Trif, M.; Loss, D. Strong Spin-Orbit Interaction and Helical Hole States in Ge/Si Nanowires. *Phys. Rev. B: Condens. Matter Mater. Phys.* **2011**, *84* (19), 195314.
(27) Wang, R.; Deacon, R. S.; Yao, J.; Lieber, C. M.; Ishibashi, K. Electrical Modulation of Weak-Antilocalization and Spin−Orbit Interaction in Dual Gated Ge/Si Core/Shell Nanowires. *Semicond. Sci. Technol.* **2017**, *32* (9), 094002.
(28) Higginbotham, A. P.; Kuemmeth, F.; Larsen, T. W.; Fitzpatrick, M.; Yao, J.; Yan, H.; Lieber, C. M.; Marcus, C. M. Antilocalization of Coulomb Blockade in a Ge/Si Nanowire. *Phys. Rev. Lett.* **2014**, *112* (21), 216806.
(29) Kloeffel, C.; Trif, M.; Stano, P.; Loss, D. Circuit QED with Hole-Spin Qubits in Ge/Si Nanowire Quantum Dots. *Phys. Rev. B: Condens. Matter Mater. Phys.* **2013**, *88* (24), 241405.
(30) Higginbotham, A. P.; Larsen, T. W.; Yao, J.; Yan, H.; Lieber, C. M.; Marcus, C. M.; Kuemmeth, F. Hole Spin Coherence in a Ge/Si Heterostructure Nanowire. *Nano Lett.* **2014**, *14* (6), 3582.
(31) Watzinger, H.; Kukučka, J.; Vukušić, L.; Gao, F.; Wang, T.; Schäffler, F.; Zhang, J.-J.; Katsaros, G. A Germanium Hole Spin Qubit. *Nat. Commun.* **2018**, *9* (1), 3902.
(32) Golovach, V. N.; Borhani, M.; Loss, D. Electric-Dipole-Induced Spin Resonance in Quantum Dots. *Phys. Rev. B: Condens. Matter Mater. Phys.* **2006**, *74* (16), 165319.
(33) Hayashi, T.; Fujisawa, T.; Cheong, H. D.; Jeong, Y. H.; Hirayama, Y. Coherent Manipulation of Electronic States in a Double Quantum Dot. *Phys. Rev. Lett.* **2003**, *91* (22), 226804.
(34) Göppl, M.; Fragner, A.; Baur, M.; Bianchetti, R.; Filipp, S.; Fink, J. M.; Leek, P. J.; Puebla, G.; Steffen, L.; Wallraff, A. Coplanar Waveguide Resonators for Circuit Quantum Electrodynamics. *J. Appl. Phys.* **2008**, *104* (11), 113904.
(35) Omelyanchouk, A. N.; Shevchenko, S. N.; Greenberg, Y. S.; Astafiev, O.; Il'ichev, E. Quantum Behavior of a Flux Qubit Coupled to a Resonator. *Low Temp. Phys.* **2010**, *36* (10), 893−901.
(36) Johansson, J. R.; Nation, P. D.; Nori, F. QuTiP 2: A Python Framework for the Dynamics of Open Quantum Systems. *Comput. Phys. Commun.* **2013**, *184* (4), 1234−1240.
(37) Benito, M.; Mi, X.; Taylor, J. M.; Petta, J. R.; Burkard, G. Input-Output Theory for Spin-Photon Coupling in Si Double Quantum Dots. *Phys. Rev. B: Condens. Matter Mater. Phys.* **2017**, *96* (23), 235434.
(38) Schuster, D. I.; Wallraff, A.; Blais, A.; Frunzio, L.; Huang, R.-S.; Majer, J.; Girvin, S. M.; Schoelkopf, R. J. Ac Stark Shift and Dephasing of a Superconducting Qubit Strongly Coupled to a Cavity Field. *Phys. Rev. Lett.* **2005**, *94* (12), 123602.
(39) Reed, M. D.; DiCarlo, L.; Johnson, B. R.; Sun, L.; Schuster, D. I.; Frunzio, L.; Schoelkopf, R. J. High-Fidelity Readout in Circuit Quantum Electrodynamics Using the Jaynes-Cummings Nonlinearity. *Phys. Rev. Lett.* **2010**, *105* (17), 173601.
(40) Boissonneault, M.; Gambetta, J. M.; Blais, A. Improved Superconducting Qubit Readout by Qubit-Induced Nonlinearities. *Phys. Rev. Lett.* **2010**, *105* (10), 100504.
(41) Bishop, L. S.; Ginossar, E.; Girvin, S. M. Response of the Strongly Driven Jaynes-Cummings Oscillator. *Phys. Rev. Lett.* **2010**, *105* (10), 100505.
(42) Bishop, L. S.; Chow, J. M.; Koch, J.; Houck, A. A.; Devoret, M. H.; Thuneberg, E.; Girvin, S. M.; Schoelkopf, R. J. Nonlinear Response of the Vacuum Rabi Resonance. *Nat. Phys.* **2009**, *5* (2), 105−109.
(43) Bruhat, L. E.; Cubaynes, T.; Viennot, J. J.; Dartiailh, M. C.; Desjardins, M. M.; Cottet, A.; Kontos, T. Circuit QED with a Quantum-Dot Charge Qubit Dressed by Cooper Pairs. *Phys. Rev. B: Condens. Matter Mater. Phys.* **2018**, *98* (15), 155313.
(44) Zajac, D. M.; Hazard, T. M.; Mi, X.; Wang, K.; Petta, J. R. A Reconfigurable Gate Architecture for Si/SiGe Quantum Dots. *Appl. Phys. Lett.* **2015**, *106* (22), 223507.
(45) Nowack, K. C.; Koppens, F. H. L.; Nazarov, Y. V.; Vandersypen, L. M. K. Coherent Control of a Single Electron Spin with Electric Fields. *Science* **2007**, *318* (5855), 1430−1433.
(46) Nadj-Perge, S.; Frolov, S. M.; Bakkers, E. P. a. M.; Kouwenhoven, L. P. Spin−Orbit Qubit in a Semiconductor Nanowire. *Nature* **2010**, *468* (7327), 1084−1087.
(47) Pribiag, V. S.; Nadj-Perge, S.; Frolov, S. M.; van den Berg, J. W. G.; van Weperen, I.; Plissard, S. R.; Bakkers, E. P. a. M.; Kouwenhoven, L. P. Electrical Control of Single Hole Spins in Nanowire Quantum Dots. *Nat. Nanotechnol.* **2013**, *8* (3), 170−174.
(48) Hu, Y.; Kuemmeth, F.; Lieber, C. M.; Marcus, C. M. Hole Spin Relaxation in Ge−Si Core−Shell Nanowire Qubits. *Nat. Nanotechnol.* **2012**, *7* (1), 47−50.
(49) Hu, X.; Liu, Y.; Nori, F. Strong Coupling of a Spin Qubit to a Superconducting Stripline Cavity. *Phys. Rev. B: Condens. Matter Mater. Phys.* **2012**, *86* (3), 035314.

NOTE ADDED AFTER ASAP PUBLICATION

This paper published ASAP on 1/17/2019. Several additional corrections were approved by the Editorial office and all of the authors, and the revised version was reposted on 1/28/2019.

DOI: 10.1021/acs.nanolett.8b04343
Nano Lett. 2019, 19, 1052−1060